Supplementary Information to: Unraveling Structure Sensitivity in CO_2

Hydrogenation over Ni

Charlotte Vogt[†], Esther Groeneveld[‡], Gerda Kamsma[‡], Maarten Nachtegaal[§], Li Lu[¥], Christopher J. Kiely[¥],

Peter H. Berben[‡], Florian Meirer[†], Bert M. Weckhuysen[†,*]

[†]Inorganic Chemistry and Catalysis group, Debye Institute for Nanomaterials Science, Utrecht University, Universiteitsweg 99, 3584 CG Utrecht, the Netherlands

[‡] BASF Nederland B.V., Strijkviertel 61, 3454 PK De Meern, the Netherlands
[Ŧ] Paul Scherrer Institute (PSI), 5232 Villigen PSI, Switzerland

[¥]Department of Materials Science and Engineering, Lehigh University, 5 East Packer Avenue, Bethlehem, PA 18015, USA

*B.M.Weckhuysen@uu.nl

SUPPLEMENTARY INFORMATION

§S.1 METHODS

Silica-supported Ni nanoparticles were created by homogeneous deposition precipitation (HDP) according to e.g. Ermakova et al[1]. The catalyst samples under investigation have varying particle sizes, as listed in Table 1.

CATALYST CHARACTERIZATION

Temperature programmed reduction (TPR) was performed in a Tristar II series analyzer. The middle of the second reduction peak (Ni(II) to Ni (0)) was chosen as the reduction temperature for each catalyst material. Per these results, all reduction steps in this work were ramped at 5 °C/min to 600 °C (catalyst A), 550 °C (catalysts B-G), and 500 °C (catalyst H), and held at these respective temperatures for 30 min.

Fresh, reduced and passivated, and spent samples were examined with transmission electron microscopy (TEM) in an FEI Tecnai12 operated at 120 kV or in an FEI Tecnai20F operated at 200 kV. Samples were crushed and suspended in ethanol under ultrasonic vibration. A drop of this suspension was deposited on a holey carbon film on a 300 mesh copper grid. Metal particle sizes listed in Table 1 under TEM are average values (>100 particles). Particle sizes were determined by TEM for fresh, reduced and spent samples (§S.2). X-ray diffraction (XRD) measurements of fresh, reduced and passivated, and spent samples were carried out in a Bruker D2 Phaser to determine crystallite size. Materials for examination by scanning transmission electron microscopy (STEM) were dry dispersed onto a holey carbon TEM grid. The catalyst samples were examined using BF- and HAADF-STEM imaging mode in an aberration corrected JEOL ARM-200CF scanning transmission electron microscope (STEM) operating at 200 kV. This microscope was also equipped with a Centurio silicon drift detector (SDD) system for X-ray energy dispersive spectroscopy (XEDS) analysis. Metal particle sizes listed in Table 1 under HAADF-STEM are surface-area averaged values (>300 particles).

Operando and ex-situ (quick-)XAS measurements were performed at beamline X10DA at the Paul Scherrer Institute in Villigen, Switzerland. The beamline was equipped with a Si(111) double crystal monochromator. A Ni foil was simultaneously measured as a reference with a third ionization chamber. For ex-situ reduction degree measurements,

the samples were reduced via the procedure described above, after which they were transferred to a quartz capillary in an N_2 glovebox, and sealed with Epotek sealant to ensure airtight transfer.

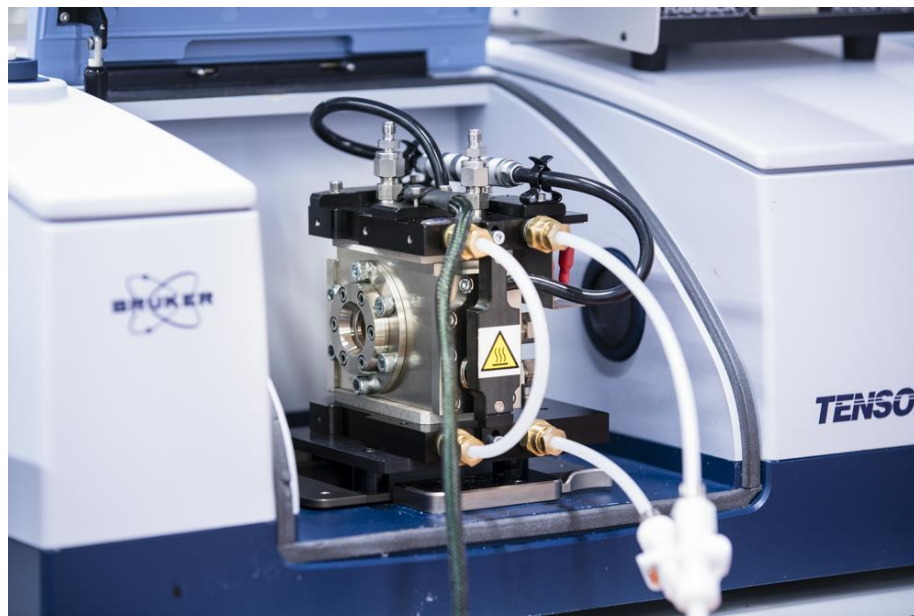## OPERANDO FT-IR WITH ON-LINE PRODUCT ANALYSIS

Figure S1. Photograph of the Specac High Temperature High Pressure operando transmission infrared spectroscopy cell in the Bruker Tensor 37 FT-IR spectrometer.

Operando Fourier transform infrared (FT-IR) spectroscopy measurements were performed to study reactants, intermediates and products in CO_2 hydrogenation over Ni. Product formation was followed by on-line gas chromatography. Time-resolved operando FT-IR spectra were recorded to study the effect of different particle sizes on reaction intermediates and catalyst activity at different temperatures. The operando FT-IR measurements were carried out using a Bruker Tensor 37 FT-IR spectrometer with a DTGS detector. Spectra were recorded every 30 s for each experiment. On-line product analysis was performed with an Interscience custom-built Global Analyzer Solutions (G.A.S) Compact $GC_{4.0}$ gas chromatograph (GC) with a time resolution of around 10 s for lower hydrocarbons (methane, ethane, and ethene).

The CO_2 hydrogenation experiments were carried out in a Specac High Temperature transmission IR reaction cell (as depicted in Figure S1). To this end, the catalyst powders were pressed into wafers of approximately 16 mm in diameter, and around 0.1 mm thickness weighing between 10-15 mg. These self-supported catalyst wafers were

created using a Specac Laboratory Pellet Press, a diaphragm vacuum pump and around 4t of pressure. Before each reaction, each catalyst was reduced at a temperature pre-determined by TPR, and reduced in-situ with a 5 °C min^{-1} temperature ramp, and a 30 min hold in a 1:1, N_2:H_2 flow with a total of 25 ml min^{-1} (both Linde, 4.9). After this in-situ reduction, the temperature of the reaction cell was brought to 100°C, and the reactants were introduced through Bronkhorst EL-FLOW Mass Flow Controllers; CO_2 at 1.25ml min^{-1}, H_2 at 5ml min^{-1} and N_2 to dilute at 6.25 ml min^{-1} for a total flow of 12.5 ml min^{-1}. In a temperature programmed reaction, the reactor was heated at a ramp of 5 °C min^{-1} to 400 °C, where the temperature was held for 90 min.

The application of operando FT-IR spectroscopy with on-line GC product analysis serves to relate CO_2 methanation activity to the presence of different gaseous and adsorbed intermediates. Structure sensitivity effects of CO_2 hydrogenation were studied with a range of different SiO_2 supported Ni catalyst particle sizes (listed in Table 1).

§S.2 CHARACTERIZATION RESULTS

EX-SITU X-RAY ABSORPTION SPECTROSCOPY

The nickel oxidation state of each of the catalyst samples under investigation (A-H) was investigated by X-ray absorption spectroscopy (XAS). Fingerprinting the Fourier transform magnitude of the phase-corrected EXAFS (R space) showed that the samples, using the reduction method as described previously, were >90% reduced, with a 10% experimental error. From fitting of the first shell, coordination numbers were obtained and are shown in Table 1 of the main text[2,3]. First shell coordination fits were done using the Artemis/Demeter software package in R space (1.9-3 Å) a DWF of 0.0087±0.00099 Å^2.
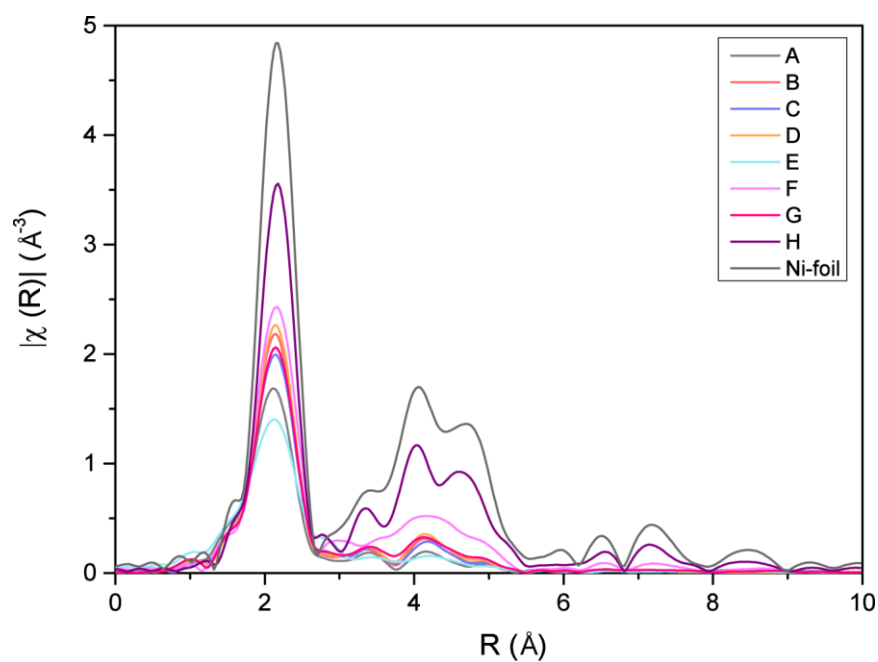
Figure S 2. Fourier transform magnitude of the phase-corrected EXAFS data of a Ni-foil reference, and the various nickel catalyst samples after the reduction procedures described.

The Fourier transform magnitudes of each sample and nickel foil in Figure S2 show a good agreement between the normalized amplitude of the first coordination shell and the particle sizes determined by other techniques. Sample E was slightly oxidized due to the ex-situ transfer of the reduced catalyst, which most likely led to the calculation of a smaller particle size with a large standard deviation in the coordination number fit.

HAADF-STEM OF POST-REDUCTION (Ni) PARTICLE SIZES

Materials for examination by scanning transmission electron microscopy (STEM) were dry dispersed onto a holey carbon TEM grid. The catalyst samples were examined using bright field (BF) and high angle annular dark field (HAADF) imaging modes in an aberration corrected JEOL ARM-200CF scanning transmission electron microscope (STEM) operating at 200 kV. This microscope was also equipped with a Centurio silicon drift detector (SDD) system for X-ray energy dispersive spectroscopy (XEDS) analysis.

The Ni/SiO_2 catalysts subjected to STEM analysis had undergone a reduction step to assure particle sizes at the beginning of the catalytic reaction. However, the Ni was subsequently re-oxidised upon exposure to air under ambient conditions during storage and transfer into the electron microscope. It was found that smaller particles ($< \sim 3$ nm in diameter) were fully oxidized to cubic NiO as shown in Figure S3 (a, b). In contrast, larger particles (> 3 nm in diameter) possessed a metallic Ni core and an oxidized shell morphology (see Figure S3(c, d). The NiO shells of the larger particles exhibited relatively uniform thickness, with a mean thickness of 1.36 ± 0.24 nm.

Hence when measuring particle size distributions by *ex-situ* methods such as TEM, STEM or XRD, we were always sampling the Ni particle after it had been fully or partially oxidised to NiO. However, we were able to correct for this effect in our STEM data, by back calculating the size of the original Ni particle that would be needed to generate a NiO or Ni/NiO core-shell particle of a certain dimension. Hence from the measured particle size distributions we were able to produce more meaningful histograms of the original Ni particle size, which would be more relevant to the catalyst under actual working conditions. These corrected Ni particle sizes were used for calculating activity and TOF values of the various catalysts.

Experimentally, the equivalent spherical diameter was taken as the particle diameter, which was deduced by measuring the 2-D projected area of the particles from HAADF-STEM images. We also took the average shell thickness, t, to be 1.36 nm. If we denote the measured diameter of the whole particle to be $d_{measured}$, and assume the lattice constants of metallic Ni and NiO to be $a_{Ni}=0.353$ nm and $a_{NiO}=0.418$ nm respectively, we can then estimate the diameter for the original metallic Ni particle as:

$$\begin{cases} \text{Fully oxidized particle } (d_{whole} \leq 2t): & d_{original} = d_{measured} \times (a_{Ni}/a_{NiO}) \\ \text{Partially oxidized particle } (d_{whole} > 2t): & d_{original} = (d_{measured} - 2t) + 2t \times (a_{Ni}/a_{NiO}) \end{cases}$$

The number of particles analyzed by STEM for each sample is listed in Table S1.

Table S1. Number of particles analyzed by HAADF-STEM.

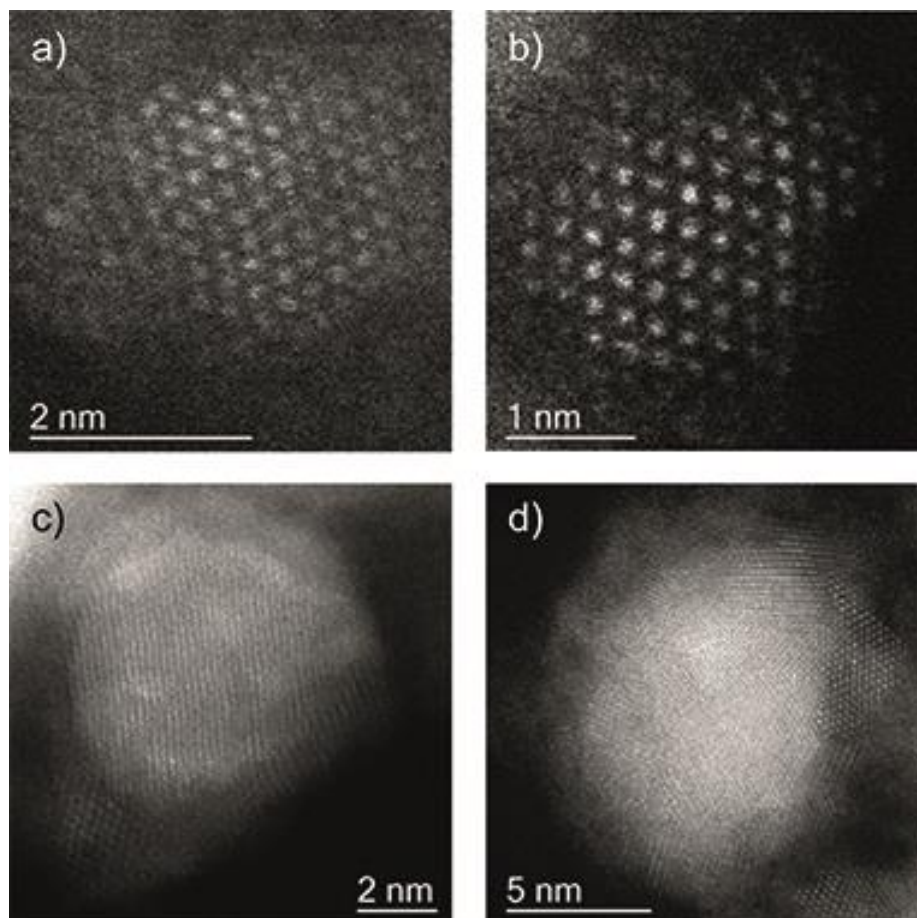| Catalyst	A	E	C	B	D	F	G	H
Ni wt%	0.95	1.7	4.7	5.0	6.7	11.8	19.5	60
Number	121	179	141	180	138	121	144	164

Figure S3. HAADF-STEM images of (a, b) Catalyst F, and G respectively fully oxidized NiO particles (both viewed from the [110] projection of cubic NiO), and (c, d) Catalyst G and H partially oxidized Ni particles.

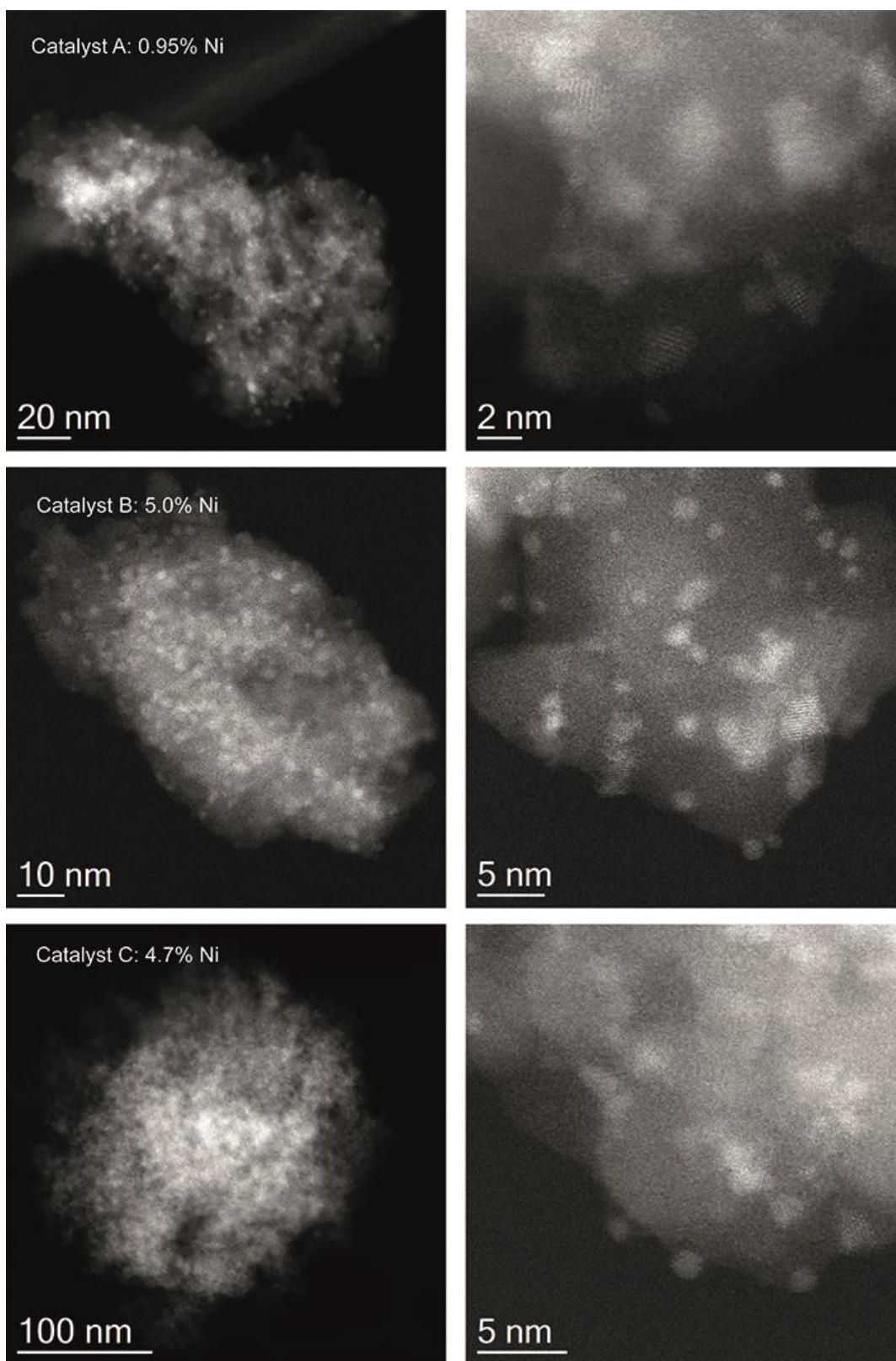**Figure S4.** Representative HAADF-STEM micrographs (lower magnification – *left column*; higher magnification – *right column)* of the Ni/SiO₂ catalyst samples A-C after their respective reduction steps, and consecutive re-oxidation under ambient conditions.

Figure S5. Representative HAADF-STEM micrographs (lower magnification – *left column*; higher magnification – *right column)* of the Ni/SiO₂ catalyst samples D-F after their respective reduction steps, and consecutive re-oxidation under ambient conditions.

Figure S6. Representative HAADF-STEM micrographs (lower magnification – *left column*; higher magnification – *right column)* of the Ni/SiO$_2$ catalyst samples G-H after their respective reduction steps, and consecutive re-oxidation under ambient conditions.
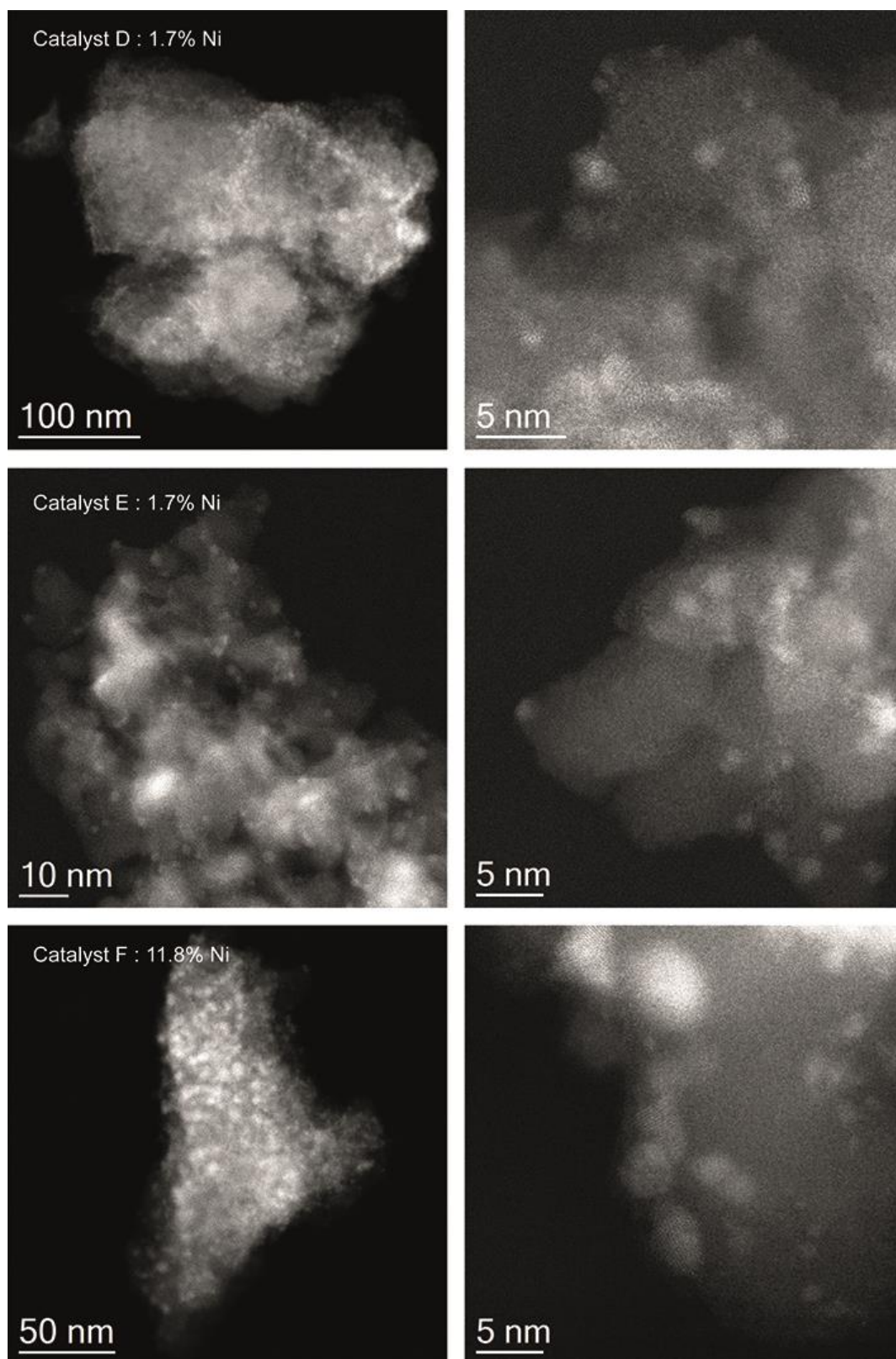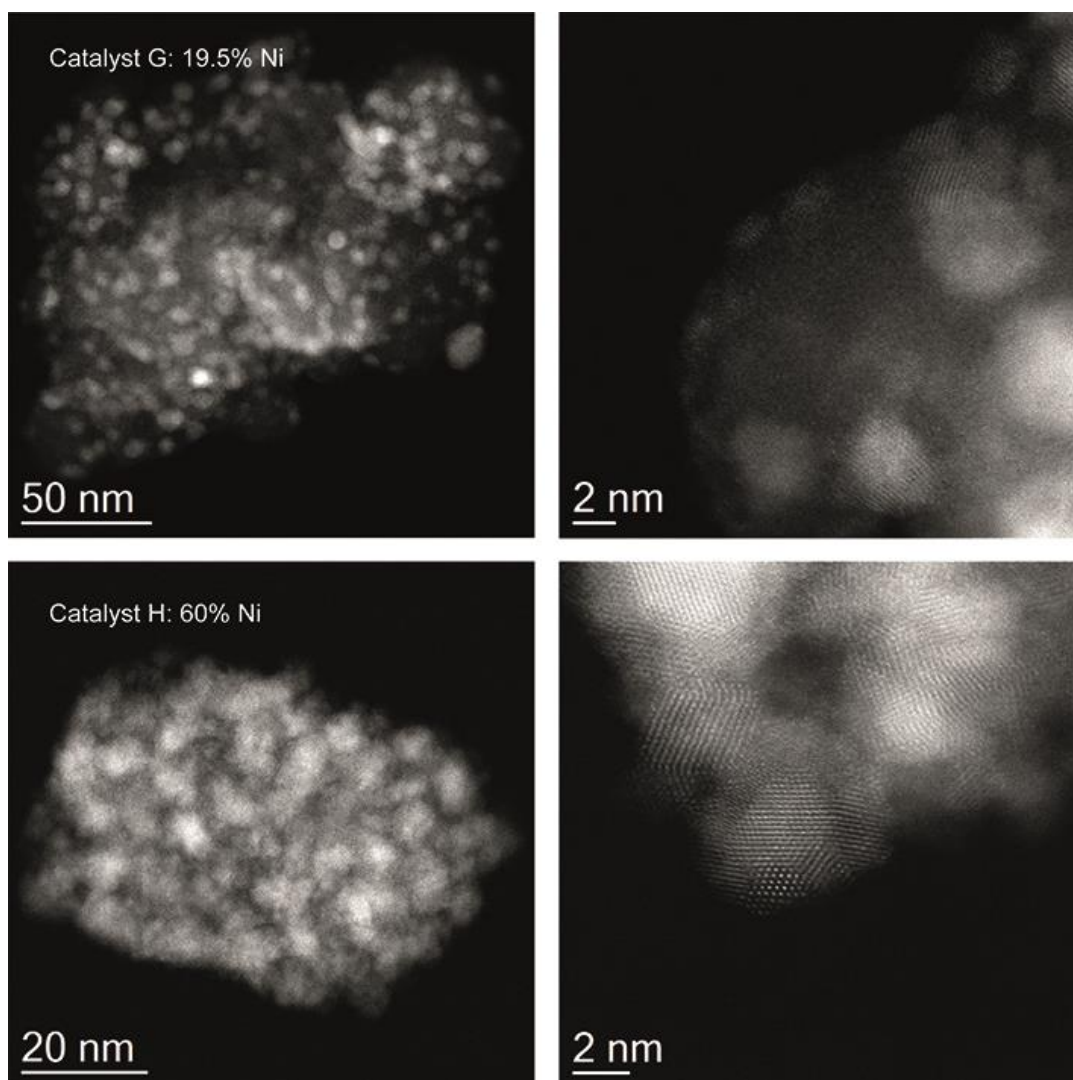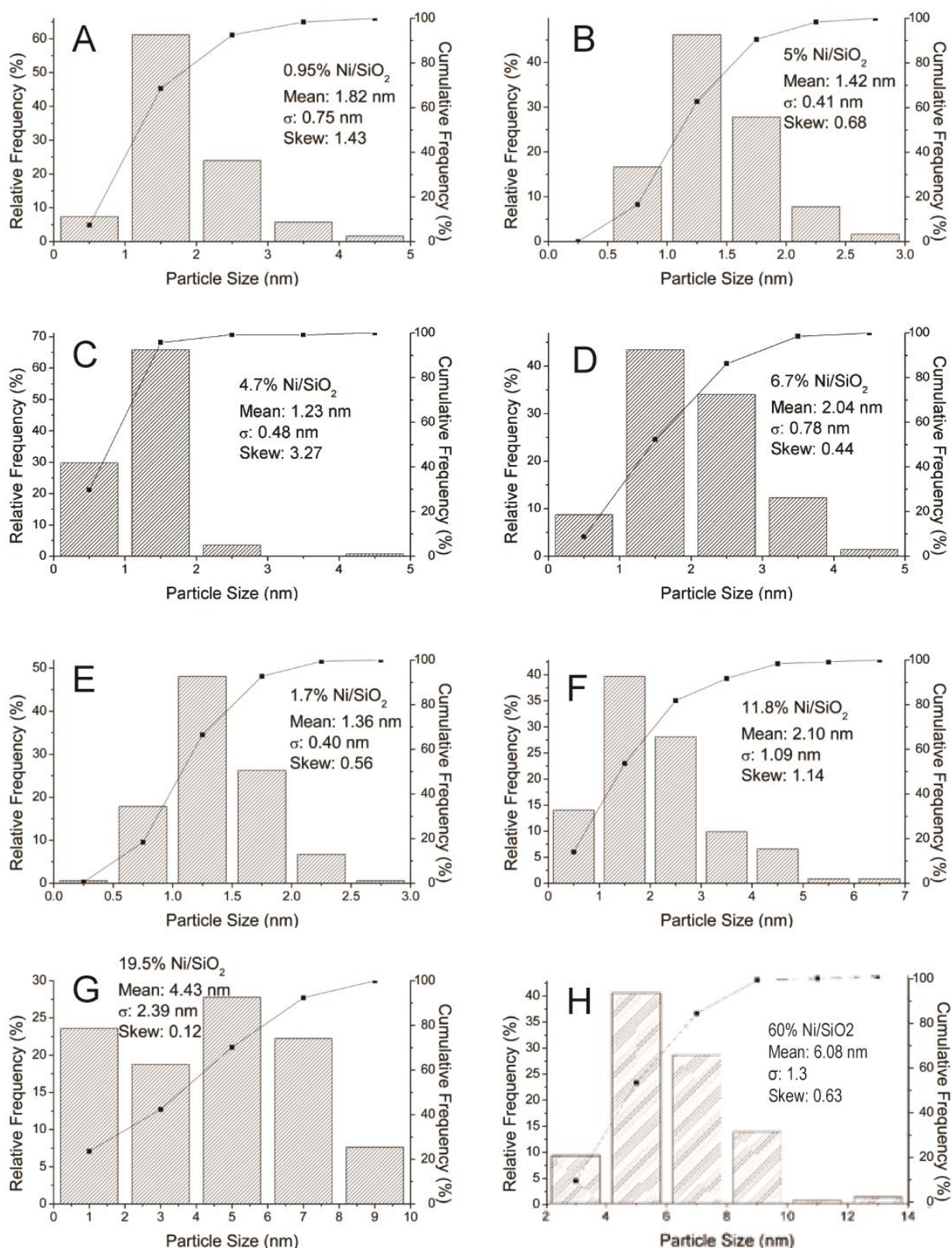
Figure S7. Particle size distributions (derived from HAADF-STEM images) of the Ni/SiO$_2$ catalyst samples A-H after their respective reduction steps, and consecutive re-oxidation under ambient conditions. These histograms have been corrected to take into the account (as described above) the full or partial oxidation of the Ni in catalyst sample. The particle size distributions shown here represent the *original Ni particle sizes* which are more relevant to the catalyst under actual working conditions

TEM OF SPENT (NiO) PARTICLE SIZES
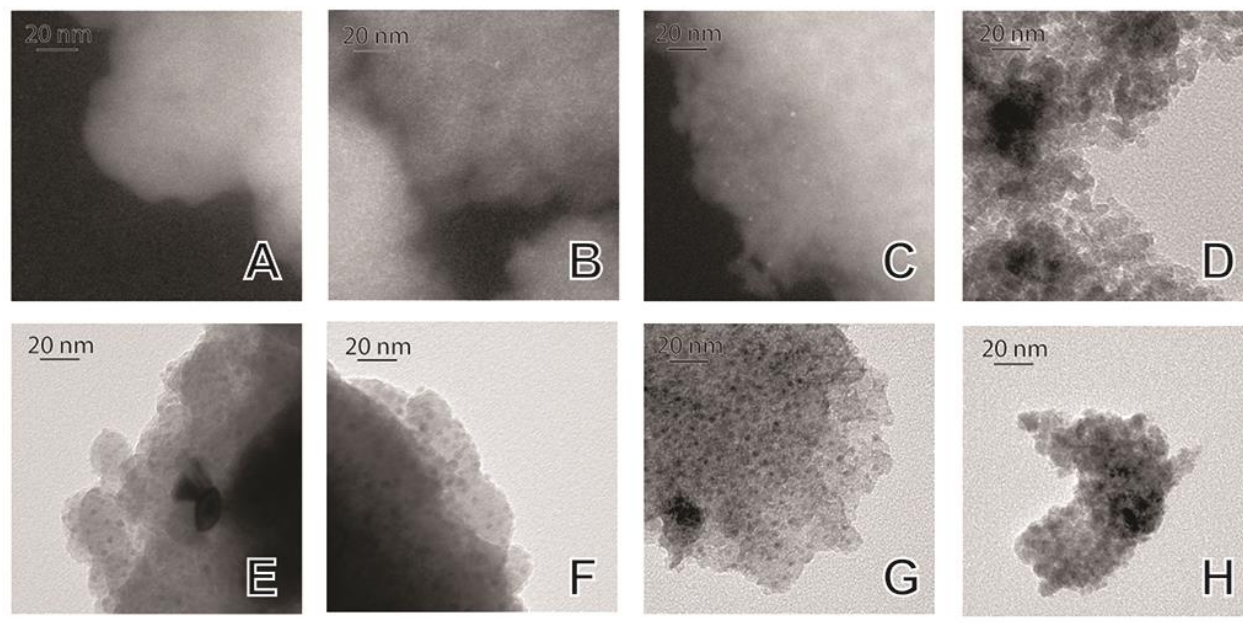
Figure S8. (DF-)TEM images of the spent catalyst samples A-H.
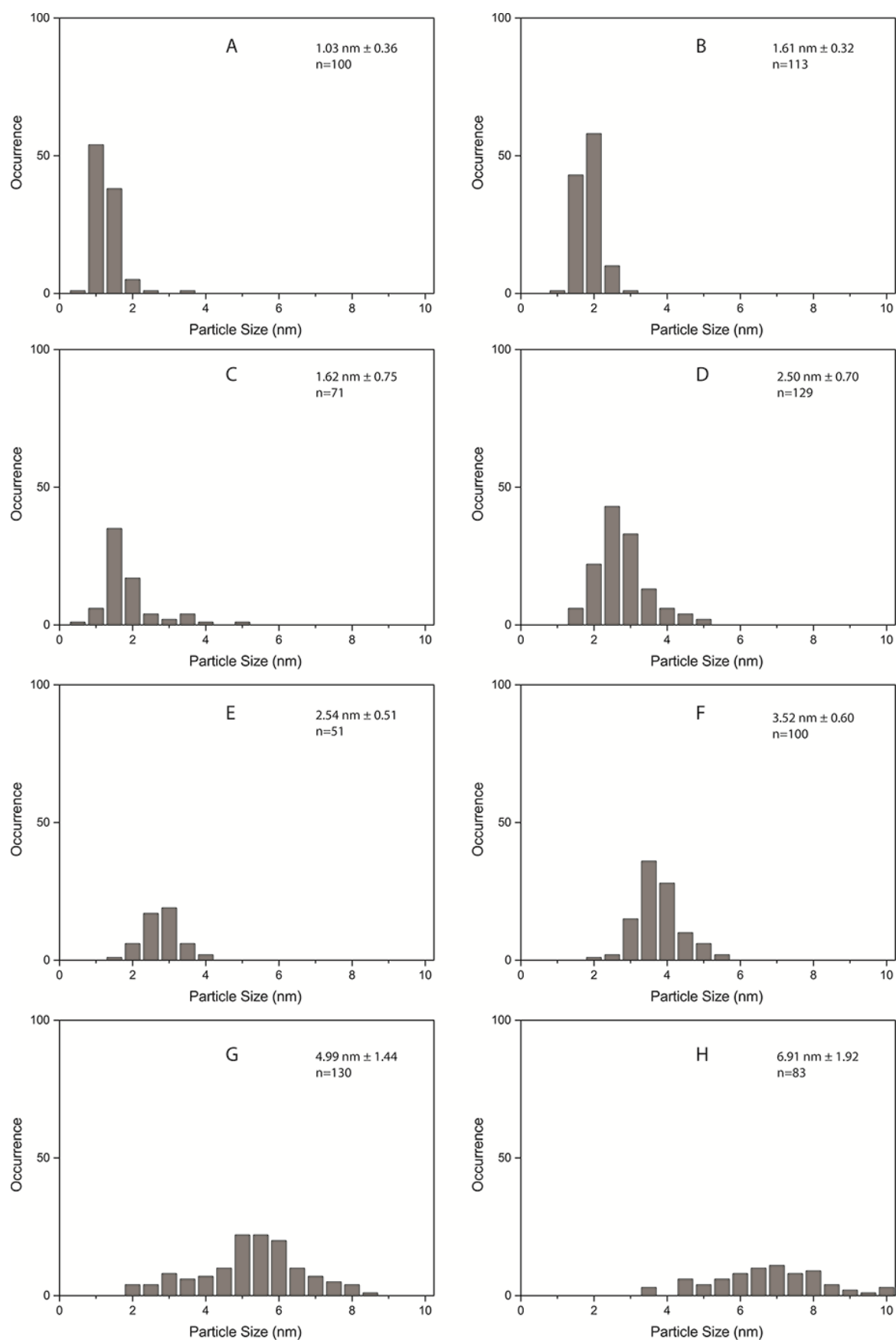
Figure S9. TEM derived particle size distributions of the spent Ni/SiO$_2$ catalysts under investigation.

§S.3 PARTICLE SIZE VS ACTIVITY RELATIONSHIPS
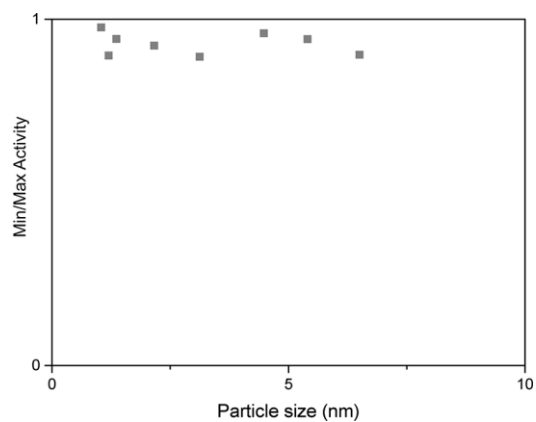
Figure S10. Deactivation set out against particle size. No clear correlation can be found between catalyst particle size and the amount of deactivation in the experiments performed and described in the main text.
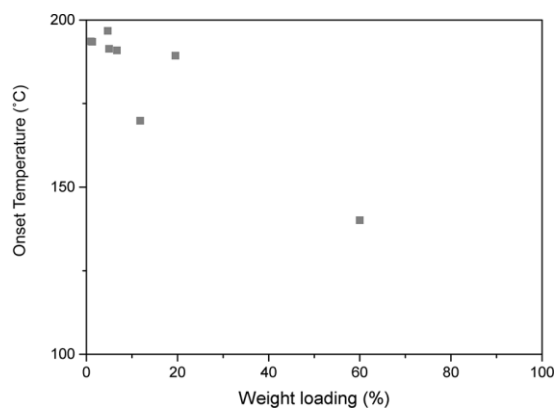
Figure S11. The initial methane production onset temperature (apparent activation energy), versus the weight loading of the Ni catalysts under investigation.

§S. 4 FT-IR STUDIES OF CATALYST SAMPLES

Table S1. Assignment of the FT-IR peaks used in this work.

Adsorption band (cm^{-1})	Species
2180 and 2095	Gaseous CO
2060	Terminally bound CO atop a single Ni (0) atom
2030	Terminally bound CO atop a single Ni (II or III) atom
1918	3-fold carbonyl species
1847	SiO$_2$ stretching vibration
1590	Conjugated C-O/C=O stretching vibration from formate species

Figures 3a and 3b in the main text show successive operando IR spectra in a typical experiment for the catalyst sample under investigation with the highest dispersion and lowest dispersion. The figures show subtracted, or difference, spectra and are focused on the adsorption region between 2250-1600 cm^{-1}, which is the region where intermediate CO$_{ads}$ species stretching vibrations occur[4–7]. The catalyst with highest dispersion shows relatively few bands in the region between 2050-1600 cm^{-1}, whereas for the catalyst with the largest Ni nanoparticles, the peaks in this region are more convoluted. This trend evolves slowly with increasing particle size, as can be seen in Figure 3 in the main text, and Figure S12a-h. Indeed, the complexity of absorption bands in the CO stretching region during CO$_2$ hydrogenation is a measure for catalyst particle size. Furthermore, the CO species adsorbed on the small catalyst particle sizes are easily flushed off, while for the large particles the species form a stable, carboxylate type intermediate.

Figure 3h in the main text displays subtracted, or difference spectra of the catalysts after reaction, flushed with 50 ml min^{-1} N$_2$ after being cooled to 50 °C. While the CO species on the catalyst with the smaller nanoparticles seem to flush off easily, the opposite is the case for larger nanoparticles. A large, broad band at around 1700-1300 cm^{-1} appears. While at first glance the peak is reminiscent to H$_2$O$_{ads}$ bending vibrations, the accompanying broad band near 3600cm^{-1} is missing which leaves us to ascribe the band to uni- or bi-dentate carboxylate groups[8]. This band only forms for the particles under study with lower dispersion, and serves to bolster the hypothesis that CO$_{ads}$ species on these catalysts are more strongly bound. That is, the lower surface coverage of CO$_{ads}$ species due to flushing with

nitrogen and decreased temperature may leave sites available to strongly bind COO species to form these uni- or bidentate carboxylates.

Figure 3i in the main text shows FT-IR spectra for experiments pulsed with labeled $^{13}CO_2$, for the catalysts under investigation with the lowest and highest dispersion. The peaks at around 1590 cm^{-1} shift to 1560 cm^{-1} under $^{13}CO_2$ feedstock, clearly the band ascribes to a carbon-containing intermediate. Conjugated C-O and C=O stretching vibrations would be expected to occur between 1500-1600 cm^{-1}. Formates, for example have a broad absorption band at around 1590 cm^{-1} on metals such as Na, and Au[9]. The full range of peaks we ascribe to CO containing intermediates red shifts by between 20-50 cm^{-1} in $^{13}CO_2$ feedstock (Figure 3i in the main text, and Supplementary Fig. S13 and 14). In addition these figures show FT-IR spectra for experiments pulsed with D_2, alternating for the usual H_2 feedstock. For the catalysts with larger particle sizes, when pulsed with D_2, a peak appears at around 1745 cm^{-1}. This is a strong indication of a H-CO or CO-H intermediate on the surface of the larger catalysts. Furthermore, the band at 1590 cm^{-1} disappears when D_2 is pulsed instead of hydrogen reinforcing the assignment of a formate-Ni species to the FT-IR peak at 1590 cm^{-1}.

It has recently been reported from theoretical work that smaller Ni particles may have more facile activation of CO_2 as they contain a higher relative amount of metal-oxide interface sites, and a synergistic effect between Ni nanoparticles and the Lewis acidity of the support is believed to exist[10]. It seems, however, that this is not the rate-determining step in CO_2 hydrogenation, nor does it account for the decreased TOF of the smallest nanoparticles (Figure 2b in the main text). Furthermore, the thermodynamic stability of the oxide of Ni-alike first row transition metal Co was calculated to have increased stability under FT conditions for sub 2 nm particles likely leading to lower activity[11]; however we show here with both FT-IR and XAS, that for Ni in CO_2 oxidation, these particles are less active because of the slow removal of charged intermediates rather than the removal of oxygen.
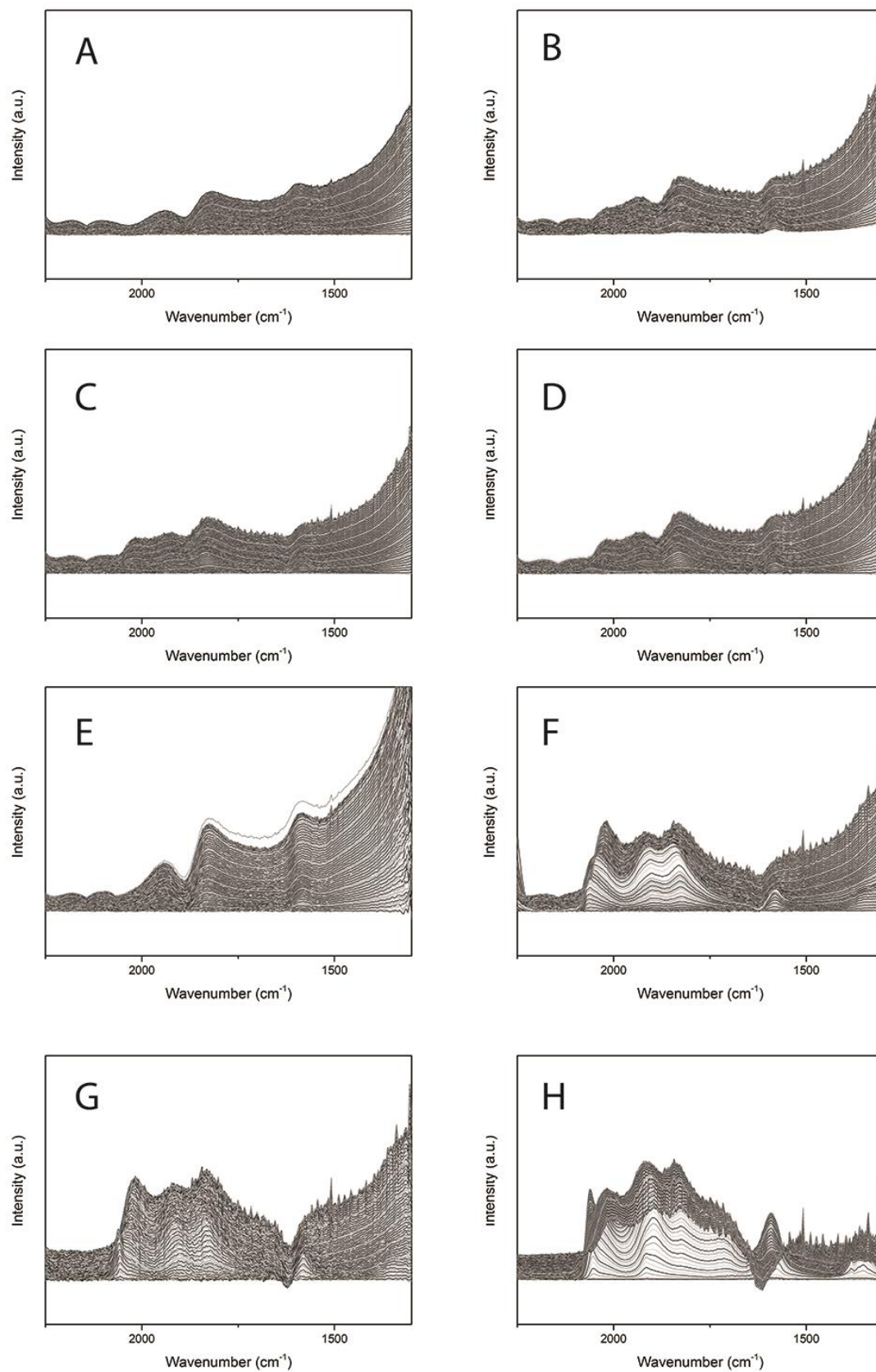
Figure S12. Operando FT-IR spectra of during CO_2 hydrogenation experiments with Ni/SiO_2 catalysts with different particle sizes, from (catalysts A-H) arranged by particle size.

As mentioned in the main text, the catalyst samples with the lowest dispersion show peaks in the CO_{ads} absorption region. These nanoparticles show a band at 2060 cm^{-1} that shifts to 2019 cm^{-1} as the reaction proceeds (Figures S12 f-h). This band is characteristic of terminally adsorbed CO atop a single Ni atom, and shifts due to the oxidation of Ni(0) to a higher oxidation state[4–7]. The presence of terminally adsorbed CO species atop a single Ni atom in the catalysts with a low relative Ni dispersion suggests a high surface coverage (i.e.; $\theta_{CO} \geq 0.57$) particularly in the beginning of the reaction[5]. Finally, the band at 1918 cm^{-1} is ascribed to bridged carbonyl species; more specifically a CO species bound to three neighboring Ni atoms. The presence of this band is expected to occur up to a surface coverage of $\theta_{CO} = 0.5$[4,5].

The peak integrations with time-on-stream as shown in Figure 3g of the main text show flat lines for sample A for the CO_{ads} peaks at 2060 and 1903 cm^{-1}. These values were artificially set to 0 as negative values were obtained as a result of our choice of baseline for integration. As Figure S15 shows, when a baseline is chosen at the minimum and maximum X-axis values of the FT-IR spectra, and contributions from SiO_2 stretching vibrations increase due to the temperature increase, a negative value is obtained. As the experiment is started with no CO_2 flow, these negative values can have no physical meaning and are truly a result of this integration procedure which is necessary for integration of the convoluted peaks between 2060-1800 cm^{-1} for samples with larger Ni nanoparticles.

Figure S13. Operando FT-IR spectra of the catalysts under investigation with the highest (black), and the lowest dispersion (grey). A solid line denotes $^{12}CO_2$ feedstock, while a dotted line denotes a $^{13}CO_2$ pulse.

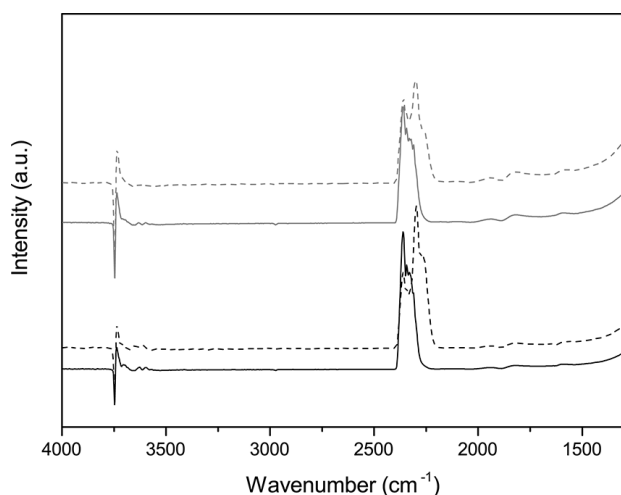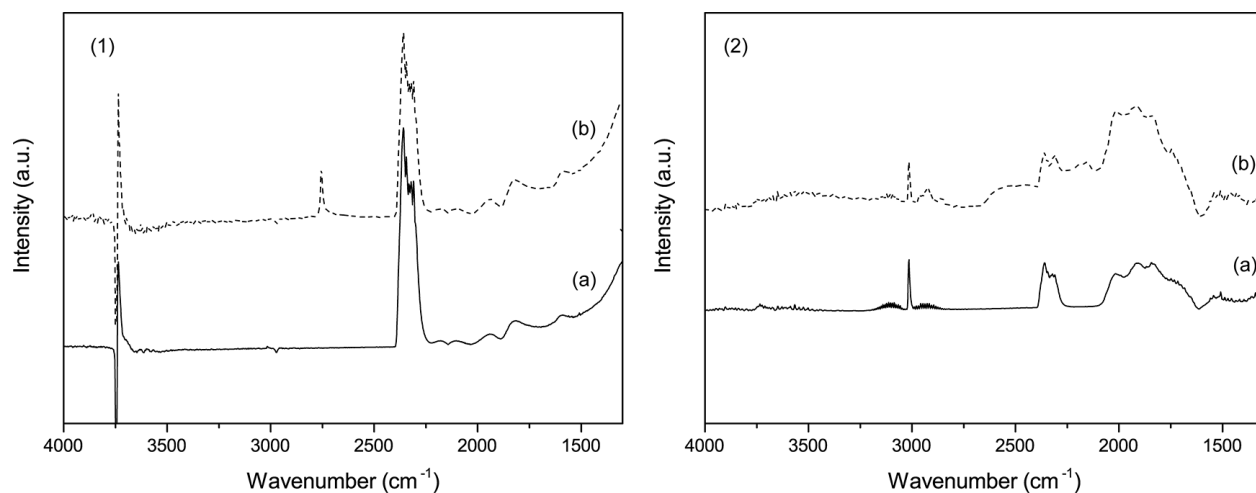**Figure S14.** Operando FT-IR spectra of the catalysts under investigation with the highest (1), and the lowest dispersion (2). A solid line denotes H$_2$ feedstock (a), while a dotted line denotes a D$_2$ pulse (b).
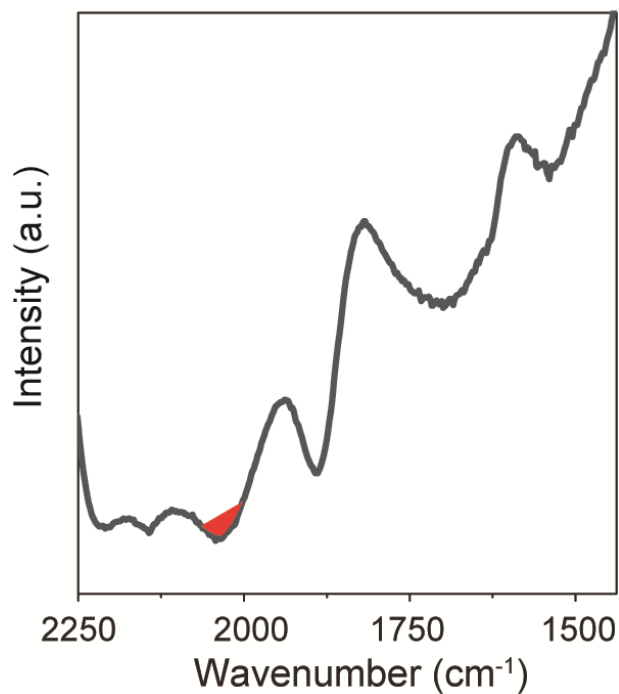

Figure S15. Figure showing the negative integration values derived from the baseline choice in the integration procedure applied in this work.

§S.5 OPERANDO QUICK-XAS

Operando quick-XAS measurements were performed in a home-built cell and set-up (see Figure S16). Powdered samples were fed into a quartz capillary and stopped with quartz wool. Graphite ferrules hold a thermocouple in place in the gas stream, and against the quartz wool ensuring a true to set temperature. Gas flows were preheated to 423K.

An automated 3-way VICI valve system was custom built to remote control the gas flows in the cell, outside of the synchrotron hutch. H_2 was attached to a single valve outlet, while N_2 and CO_2 together were connected to a single valve outlet. While tubing was minimalized around the cell, trace amounts of CO_2 remained in the first N_2 flow, and vice versa.
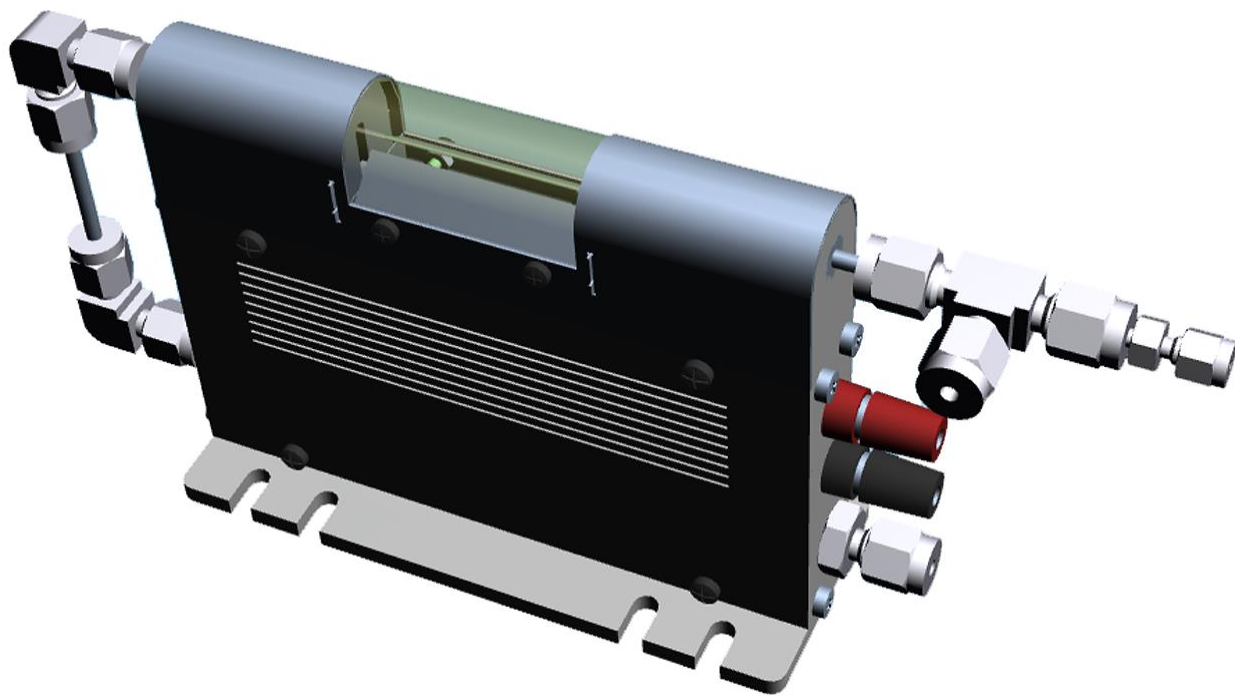

Figure S16. Schematic of the operando capillary cell used for operando Q-XAS[19].

One X-ray absorption spectrum was recorded every 100 ms (Figure S17) and the data was binned per 40 spectra, to 4 s time resolution to improve the signal to noise ratio. The resulting spectra were normalized and then subjected to

principal component analysis (PCA) and clustering to further reduce the noise level. This was necessary to achieve sufficient sensitivity to detect the subtle changes in oxidation state, which occur during reaction. To illustrate the validity of this approach, least squares linear combination fitting (LSLC) of each individual X-ray absorption near edge structure (XANES) with NiO[12] and Ni metal references (i.e. without using any binning, PCA, and clustering), is plotted in Figure S18 against time on stream for each experiment. At this time resolution (100 ms) the noise level is too high to observe the subtle features during oxidation and re-reduction of the catalyst, which illustrates the necessity for noise reduction. However, a simple smoothing procedure (moving average with a span of 66 data points, i.e. 6.6 s) allowed us to obtain a similar signal to noise ratio as obtained by the approach using PCA and clustering (see Figure S19 and Figure 4 of the main text), but obviously with a clear loss in time resolved features. Most importantly, the conclusions we draw from the data and are discussed in the main text (i.e. more oxidation for smaller particle sizes, and the availability of sites with different activity) still hold when examining the LSLC data as presented in Figures S14 and S15.
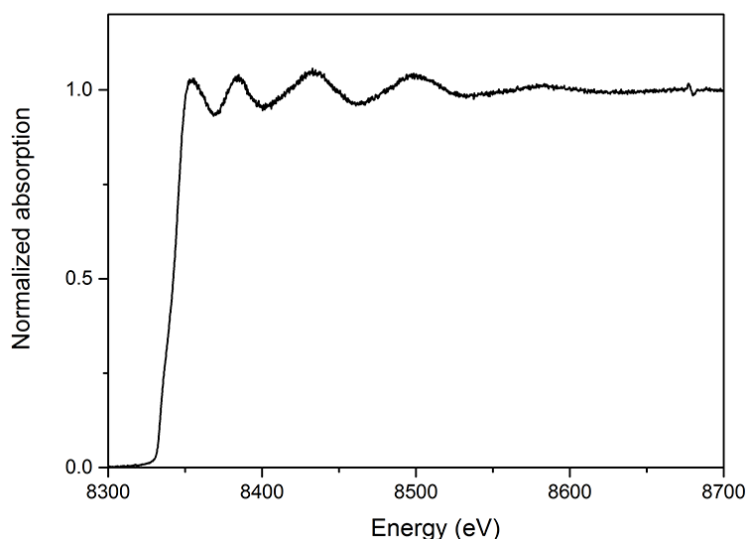
Figure S17. Single normalized spectrum (i.e., recorded every 100 ms).

In the approach using PCA and clustering the time series of spectra is treated as a matrix of size T x E where T represent the number of spectra (one per time stamp, i.e. every 4 s) and E the number of X-ray energies of each X-ray absorption spectrum. First PCA was used to reduce the dimensionality of this E-dimensional data space using singular value decomposition (SVD) of the data matrix, while preserving the relevant information, by describing the data in a way that best explains the variance of the entire data set[13,14]. It is important to note that the principal

components (PCs) do not represent pure chemical states (here Ni or NiO) but are linear combinations of the E independent variables and provide a new orthogonal basis set that optimally describes the data in terms of its variance. PCA further sorts these PC according to the level of variance associated with each PC. Therefore, the data can be represented by a new matrix, $T \times PC_{1...E}$, which can then be reduced to $T \times PC_{1...N}$ without losing important information by choosing the first N principal components. Because PCs are aligned to best describe the spread in the data, projecting the latter to this new N-dimensional PC space (score plot) highlights pattern (here correlations in time) in the data and effectively reduces noise, which is now described by PCs having indices larger than N. In this work using the first two PCs was found sufficient to achieve an effective noise reduction without losing important information. The distance between data points in the score plot is a direct measure of the similarity of the X-ray absorption spectra, that is, in this case the oxidation state of Ni. Therefore, k-means clustering[15,16] of the data points in the reduced PC space (i.e. the score plot) was performed, grouping pixels according to their (Euclidean) distances from cluster centers (centroid linkage method). This initial clustering result was refined (using the result from k-means clustering as initial guess) by subsequent Gaussian mixture modeling (GMM) using an expectation maximization (EM) algorithm[17]. The result of this clustering refinement provides the same number of clusters but is based on the point density in PC space and because the distribution is described by a set of overlapping Gaussians, each data point (spectrum in time) is assigned a class membership value, indicating the degree to which it belongs to a certain cluster. The latter is especially useful as it allows calculating a weighted average X-ray absorption spectrum for each cluster, using this class membership value as a weight for each spectrum. Here we need to point out that the number of clusters does not necessarily need to represent the number of pure phases (here 100% Ni and NiO) but will simply segment the data points in PC space into k groups of most similar spectra. Because we expected a gradual change between the two pure states Ni and NiO we intentionally over-clustered the data into 6 clusters in turn achieving a less coarse segmentation of the data into 6 groups if differing percentages of pure Ni and NiO. This was confirmed by fitting the weighted average of all XANES belonging to each cluster (Figure S20) using LSLC fitting with NiO[12] and Ni metal references, i.e. following the same approach as above but fitting only the 6 spectra belonging to each cluster instead of fitting each (non-binned) individual spectrum of the time series.

Inspection of the near edge features and the edge shift of each group's X-ray absorption spectrum showed a different degree of reduction/oxidation for each group. A quantitative value for each cluster indicating the degree of reduction expressed as the ratio of Ni metal relative to NiO was thereby obtained for each cluster. Finally, the class

membership value (i.e. how much each individual spectrum belongs to each of the clusters) of each individual spectrum of the time-resolved experiment was combined with the result of the LSLC fit to determine for each time step the degree of reduction (expressed as percentage of metallic nickel in Figure 4) showing its evolution with time-on-stream. Fitting errors (Ni metal % ± 0.011-0.012) were approached by variation of the fitting region in the Athena software package. The changes we observe fall into the order of magnitude of this fitting error, however as this is not a random error, the mean percentages for the attribution of Ni metal versus NiO reference will shift together. Thus the order of magnitude of changes in oxidation state is likely to remain what we report. That is, fitting with pure NiO and Ni metal references shows that the changes in the clustered spectra we observe will remain at no more than around 2.3% change in overall oxidation state for the smallest Ni nanoparticle size.

We conclude that this analysis approach allowed us to increase the signal to noise ratio significantly with respect to e.g. pure LSLC fitting, by eliminating correlated and random noise. For a bulk technique such as Q-XAS, eliminating contributions from random noise is imperative to detect and correlate the subtle surface changes in active sites such as described in this work.
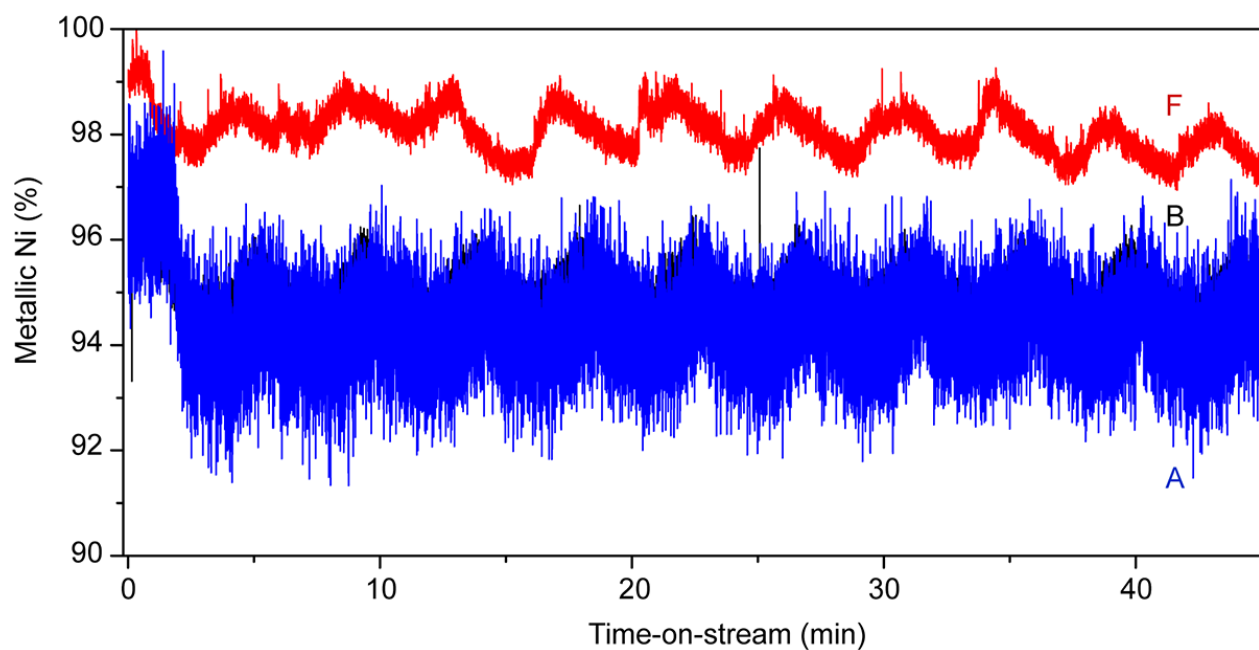

Figure S18. Result of LSLC Fitting with NiO and Ni metal reference of each individual spectrum plotted against time-on-stream.
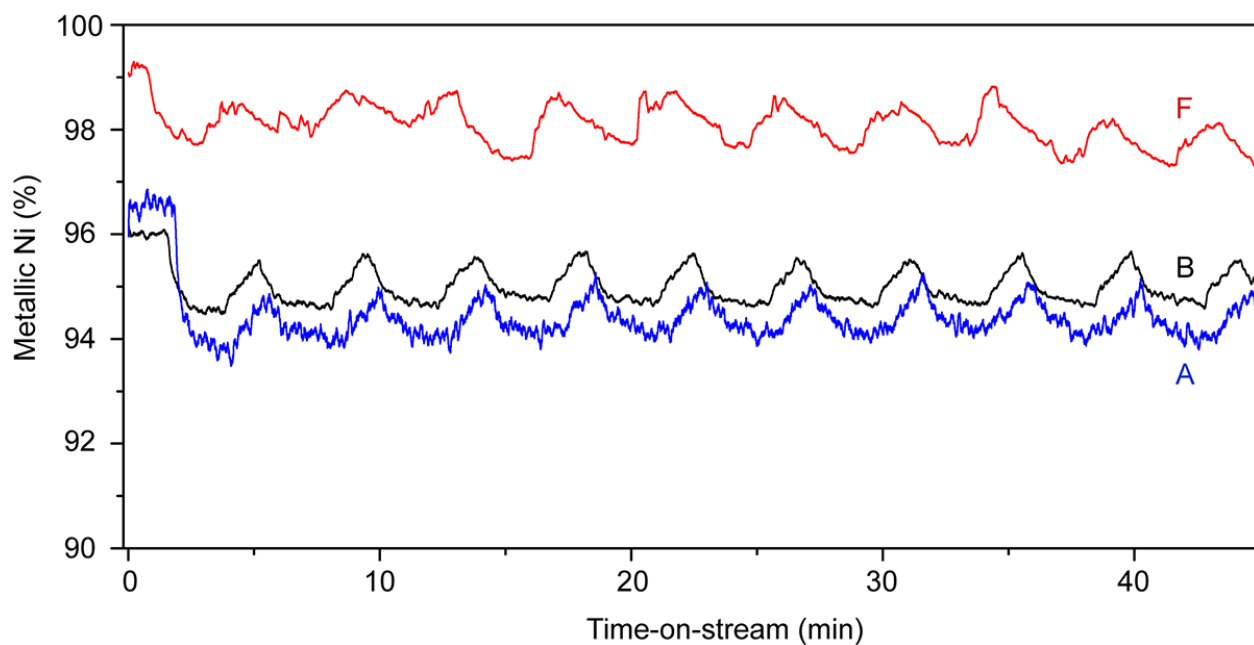
Figure S20. Result of LSLC Fitting with NiO and Ni metal reference of each individual spectrum plotted against time-on-stream, smoothed by 66 data points.
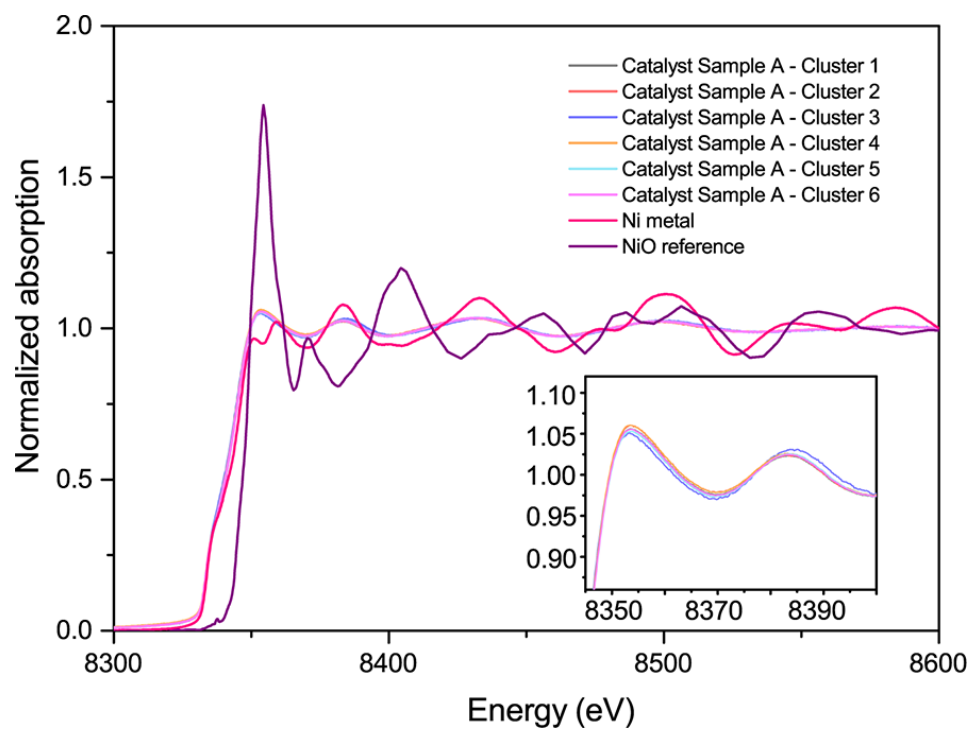

Figure S19. X-ray absorption spectra (cluster 1-6) calculated as the weighted average of all spectra of the group using the class membership value of each spectrum determined during clustering.

§S.6 QUANTIFICATION OF QXAS RESULTS

The atoms in a unit cell of (111) surface is $S = \frac{1}{2}a^2\sqrt{3}$, with an atom density of $\frac{2}{0.866}a^2$ [18]. For a (100) surface, the atom density is $\frac{2}{a^2}$, and for a (110) surface, the atom density is $\frac{2}{1.414*a^2}$ [18]. With a lattice constant (a) of 3.52 for Ni, the average of these three densely packed surfaces amounts to $1.62*10^{15}$ cm^{-1}. The number of atoms per cm^3 can generally be written as the density of the metal divided by the atomic weight multiplied by Avogadro's constant, or $\frac{\rho}{Mw}N_{av}$, equaling $1.09*10^{-23}$ cm^3 per nickel atom. The dispersion for Ni according to these principles is plotted in Figure S21, showing the total amount of Ni atoms in a nanoparticle, along with the amount of surface atoms at a given diameter. In grey is the dispersion, or ratio of atoms at the surface.
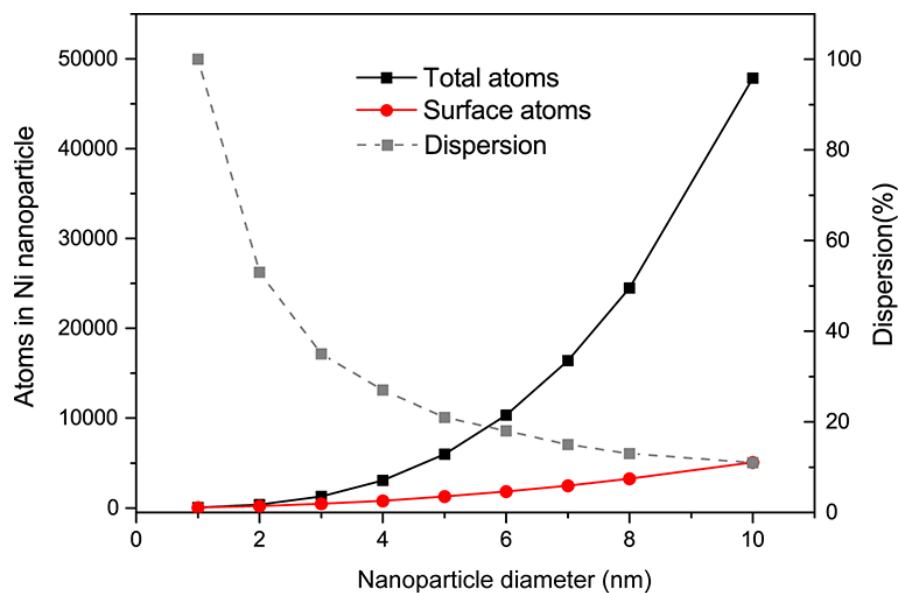

Figure S21. Amount of total Ni atoms in a nanoparticle versus atoms at the surface, and their dispersion.

The changes in oxidation state we observe with our QXAS experiments are minimal. We have assessed if any contributions from oxygen impurities in the CO_2 may have caused the observed oxidation state changes, rather than actual activation of CO_2. The evidence for the latter is two-fold; first is that the Ni surface oxidation state changes cannot be not caused by trace levels of oxygen in the CO_2, as there is simply not enough O_2 to account for the changes we observe. That is; with the weight of the samples in the capillary plug flow reactor (0.0018 g for catalyst A, 0.0029 g for catalyst B, and 0.0023 g for catalyst F), and the particle sizes determined by HAADF-STEM, the

amount of particles (assuming hemispheres) can be calculated ($2.2 \cdot 10^{15}$, $2.15 \cdot 10^{16}$, and $2.08 \cdot 10^{16}$, resp.). With oxidation state changes in Q-XAS of 1.5%, 1.5% and 2.3% for catalysts A, B, and F, respectively, and 315, 192 and 545 atoms in a particle; that means that 3, 2 and 5 atoms would be oxidized for catalysts A, B, and F, respectively. The amount of particles multiplied by the amount of atoms that are oxidized during the pulses gives the total amount of Ni atoms that are oxidized during the 100s CO_2 pulse ($3.65 \cdot 10^{15}$, $4.3 \cdot 10^{16}$ and $1.04 \cdot 10^{17}$, resp.). Assuming an ideal gas, 1 ml/min CO_2 flow would give $4.4 \cdot 10^{-5}$ moles of CO_2, of which maximally $0.8 \cdot 10^{-11}$ (AirLiquide CO_2 at N48 purity) could be oxygen atoms.

Assuming the maximum amount of oxygen impurities were present in the gas, and all oxygen atoms that were present actually oxidized the nickel surface, only 0.08% of the surface changes could be accounted for by oxygen for catalyst F in which we see e.g. clear plateau formation, 0.21% for catalyst B, to maximally 2.42% in catalyst A which gave noisy spectra and clustering results also due to the sample's low weight loading.
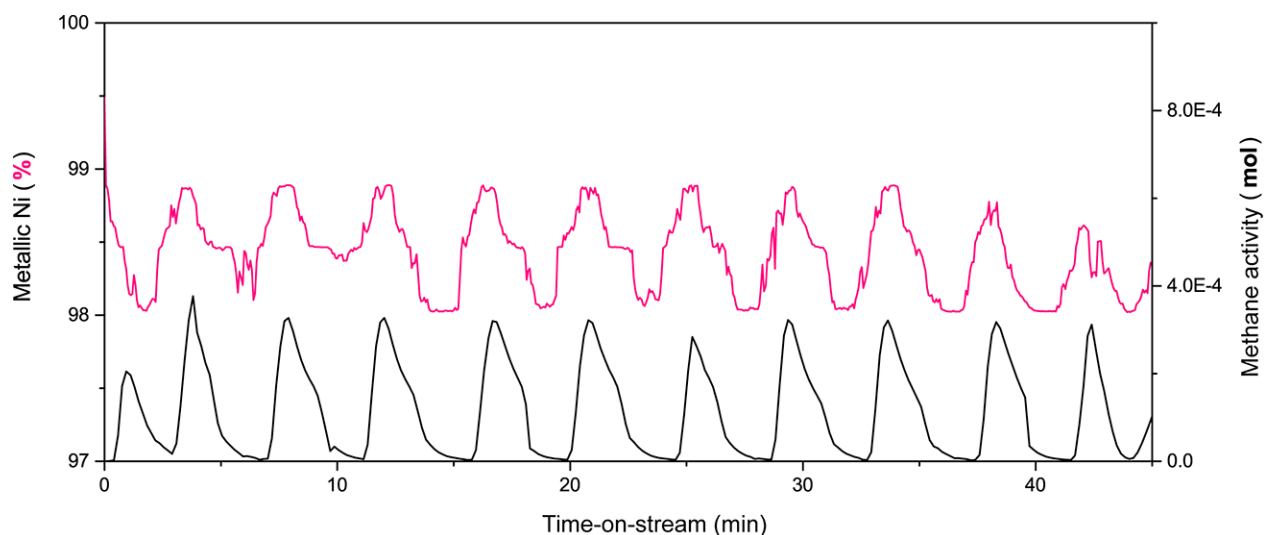
Figure S22. Results of PCA and clustering approach for Q-XAS data plotted along with methane activity measured in operando for catalyst F.

Secondly, during the CO_2 pulses, methane was formed as evidenced by GC measurements plotted in Figure S22 for catalyst F. In order for methane to form on the surface, CO_2 has to be split or activated. One could assume that all the O_{ads} and CO_{ads} first formed from CO_2 splitting would form water and methane with the availability of any hydrogen

left on the surface, and that when the hydrogen is used up, CO_2 would start to oxidize the surface. While it may seem that this could also account for the plateau formation in XAS results plotted in Figure 4 of the main text, methane formation during these pulses also seems correlated to the oxidation state changes as shown in Figure S22 for catalyst F. If methane were to form purely due to the hydrogen that is present on the surface, with no regard to different sites with different activity; the pulse of methane that would be created would be instantaneous, while the pulse we measure in GC as plotted in Figure S22 actually shows the two step speed of formation of methane. That suggests that truly, there are two different sites with different activity present on the catalyst particle. Last, it's important to note that the order of methane production to oxidized atoms is an order of magnitude of 2 to 3 larger. I.e., 10 to 100x more molecules of methane are produced than the amount of atoms which oxidize during the reaction. This further suggests that there are different mechanisms and sites with different activity on the different nanoparticle sizes.

§S.7 REFERENCES

1.   Ermakova, M. A. & Ermakov, D. Y. High-loaded nickel-silica catalysts for hydrogenation, prepared by sol-gel route: structure and catalytic behavior. *Appl. Catal. A Gen.* **245,** 277–288 (2003).

2.   Chumakova, A. V. *et al.* Periodic order and defects in Ni-based inverse opal-like crystals on the mesoscopic and atomic scale. *Phys. Rev. B - Condens. Matter Mater. Phys.* **90,** 1–9 (2014).

3.   Frenkel, A. I., Hills, C. W. & Nuzzo, R. G. A view from the inside: Complexity in the atomic scale ordering of supported metal nanoparticles. *J. Phys. Chem. B* **105,** 12689–12703 (2001).

4.   Camputano, J. C. & Greenler, R. G. The adsorption sites of CO on Ni(111) as determined by infrared reflection - absorption spectroscopy. *Surf. Sci.* **83,** 301–312 (1979).

5.   Trenary, M., Uram, K. J. & Yates, J. T. An infrared reflection-absorption study of CO chemisorbed on clean and sulfided Ni(111) - evidence for local surface interactions. *Surf. Sci.* **157,** 512–538 (1985).

6.   Layman, K. A. & Bussell, M. E. Infrared spectroscopic investigation of CO adsorption on silica-supported nickel phosphide catalysts. *J. Phys. Chem. B* **108,** 10930–10941 (2004).

7. Courtois, M. & Teichner, S. J. Infrared studies of CO O_2 and CO_2 gases and their interaction products, chemically adsorbed on nickel oxide. *J. Catal.* **135,** 121–135 (1962).

8. Socrates, G. *Infrared and Raman Characteristic Group Frequencies*. (Wiley, 2001).

9. Filonenko, G. A. *et al.* The impact of metal-ligand cooperation in hydrogenation of carbon dioxide catalyzed by ruthenium PNP pincer. *ACS Catal.* **3,** 2522–2526 (2013).

10. Silaghi, M., Comas-Vives, A. & Copéret, C. CO_2 activation on Ni/γ-Al_2O_3 catalysts by first-principles calculations: from ideal surfaces to supported nanoparticles. *ACS Catal.* **6,** 4501–4505 (2016).

11. Van Steen, E. *et al.* Stability of nanocrystals: Thermodynamic analysis of oxidation and re-reduction of cobalt in water/hydrogen mixtures. *J. Phys. Chem. B* **109,** 3575–3577 (2005).

12. Meirer, F. *et al.* Three-dimensional imaging of chemical phase transformations at the nanoscale with full-field transmission X-ray microscopy. *J. Synchrotron Radiat.* **18,** 773–781 (2011).

13. Jolliffe, I. T. *Principal Component Analysis, Second Edition*. *Principal Component Analysis* (Springer, New York, 2002). doi:10.2307/1270093

14. Jackson, J. E. *A User's Guide to Principal Components*. (Wiley-Interscience, Hoboken, New Jersey, 2003).

15. MacQueen, J. B. *5th Berkeley Symposium on Mathematical Statistics and Probability*. (University of California Press, Berkeley, CA, 1967).

16. Johnson, R. A. & Wichem, D. W. *Applied Multivariate Statistical Analysis*. (Pearson, Upper Saddle River, New Jersey, 2002).

17. Bishop, C. *Pattern Recognition and Machine Learning*. (Springer-Verlag, New York, 2006).

18. Atkins, P. *et al. Inorganic Chemistry*. *Library* (W. H. Freeman and Company, New York, 1999).

19. Fischer, N., Clapham, B., Feltes, T., Van Steen, E. & Claeys, M. Size-dependent phase transformation of catalytically active nanoparticles captured in situ. *Angew. Chem. - Int. Ed.* **53,** 1342–1345 (2014).